arXiv:1703.05630v1 [cs.CV] 16 Mar 2017

Anisotropic-Scale Junction Detection and Matching for Indoor Images

Nan Xue[1],Gui-Song Xia[1], Xiang Bai[2], Liangpei Zhang[1], Weiming Shen[1],
[1]*State Key Lab. LIESMARS, Wuhan University, Wuhan, China.*
[2]*Electronic Information School, Huazhong University of Science and Technology, China.*

Abstract

Junctions play an important role in the characterization of local geometric structures in images, the detection of which is a longstanding and challenging task. Existing junction detectors usually focus on identifying the junction locations and the orientations of the junction branches while ignoring their scales; however, these scales also contain rich geometric information. This paper presents a novel approach to junction detection and characterization that exploits the locally anisotropic geometries of a junction and estimates the scales of these geometries using an *a contrario* model. The output junctions have anisotropic scales — i.e., each branch of a junction is associated with an independent scale parameter — and are thus termed *anisotropic-scale junctions* (ASJs). We then apply the newly detected ASJs for the matching of indoor images, in which there may be dramatic changes in viewpoint and the detected local visual features, e.g., key-points, are usually insufficiently distinctive. We propose to use the anisotropic geometries of our junctions to improve the matching precision for indoor images. Matching results obtained on sets of indoor images demonstrate that our approach achieves state-of-the-art performance in indoor image matching.

Image correspondence is a key problem for many computer vision tasks, such as structure from motion [1–4], object recognition [5,6] and many others [7,8]. Recent decades have witnessed great successes in addressing this problem that have been achieved by detecting and matching local visual features [9–13]. Although most existing image matching algorithms that rely on such local visual features perform well for images that contain rich photometric information, e.g., outdoor images, they typically lose efficiency on images that are less photometric and dominated by geometric structures, such as the indoor images displayed in Fig. 1. In indoor scenarios, images are often dominated by low-texture regions and show dramatic changes in viewpoint; it has been reported that in such cases, it is more effective to seek correspondences between geometric structures [14,15], such as line segments [16,17] and junctions [18].

The line segment matching problem has been studied in recent years because line segments represent more structural information than key-points. Many algorithms use either photometric descriptors for individual line segments [19] or the underlying geometric relation [14,15] to assist in line segment matching. Approaches based on pre-estimated epipolar geometries usually perform better than those that use photometric descriptors [19], but epipolar geometry estimation still requires key-point correspondences in many situations. For indoor scenes, because the descriptors for low-textured regions are not sufficiently distinctive, it is very likely that the epipolar geometry produced for use in line segment matching will be unstable. It is therefore of great interest to develop elegant ways to find the correspondences between geometric structures in images while eliminating the errors introduced by key-point correspondences to ultimately achieve better matching of indoor images.

Alternatively, junctions, as a type of basic structural visual feature, have been studied as features of primary importance for perception and scene understanding in recent years [20–22]. As combinations of points and ray segments, junctions contain richer information than line segments; a junction includes a location and at least two ray segments (known as *branches*). Ideally, the information contained in a pair of junctions

Figure 1: A pair of indoor images. These images are dominated by geometric structures, e.g., the edges of the door, and a low-textured wall.

should enable us to recover the correspondences between images in the form of affine transformations. However, because of the difficulties encountered in estimating the endpoints of junction branches, most junction detection algorithms [23–28] concentrate on identifying only the junction locations and the orientations of the branches while ignoring their lengths. This approach effectively simplifies junctions to key-points and does not fully exploit their potential for revealing image correspondences. To enable better characterization of the structure of junctions, the ACJ detector [28] estimates scale-invariant junctions; such a junction is represented isotropically as a circular region with two or more dominant orientations. Every orientation represents a branch of the junction, and the radius of the circle is equal to the shortest length among these branches. Although the orientations of the branches are invariant with respect to the viewpoint, this information is not sufficient for estimating affine transformations. Fortunately, however, if we can estimate the length of every branch, then a correct affine transformation can be determined from a corresponding pair of junctions.

Motivated by this possibility, we wish to study how to exploit the invariance of junctions by estimating the scales (lengths) of their branches. For indoor images, the inherent scales of junctions are usually the lengths of certain (straight) boundaries of salient objects in the images, which contain rich structural information that extends beyond the information provided by local features. More precisely, we propose an *a contrario* approach in which the endpoints of a ray segment are modeled starting at a given location with initial orientations, and for each proposed point, it is checked whether that point should be considered part of the ray segment based on the *number of false alarms* (NFA). Points that belong to a given ray segment are continuously identified until the continuity is broken, which allows the inherent scale of that ray segment to be determined. In reality, the initial orientations are noisy; therefore, we also optimize them in terms of their junction-ness based on the *a contrario* theory. Once the anisotropic scale has been estimated for each branch (ray segment), a local homography can be estimated from any corresponding pair of junctions extracted from two different images. Theoretically, a correct correspondence will produce a reasonable local affine homography, whereas incorrect correspondences will generate inaccurate local homographies. Considering the certainty of the junction locations, the regions around each location can be mapped using the (correct or incorrect) affine homographies identified in this way. Correct homographies will map one image to the other with minimal patch distortion. The mapping of a corresponding pair of image regions using the affine homography inferred from the corresponding pair of junctions can be used to check whether that pair of junctions represents a true correspondence. When the corresponding junctions are correctly identified in an image pair, the results will provide rich structural information. Our contributions in this paper are as follows:

- We extend the junction detector presented in [28] to anisotropic-scale geometric structures, which can better represent the geometric information contained in indoor images.
- We develop an efficient scheme for identifying the correspondences between *anisotropic-scale junctions* (ASJs). More precisely, because a detected ASJ consists of at least three points, each pair of matching

junctions between two images induces an affine homography. Finally, we present a strategy for using these induced homographies to generate accurate and reliable correspondences between the locations and anisotropic branches of junctions simultaneously.

- We evaluate our method on challenging indoor image pairs (e.g., some images are taken from the indoor image datasets used in [29, 30]), and our results demonstrate that the proposed method can achieve state-of-the-art performance in matching indoor images.

The remainder of this paper is organized as follows. First, the existing research related to our work is reviewed in Sec. 1. In Sec. 2, the problem of detecting and matching junctions for an indoor scene is discussed. In the subsequent section, an *a contrario* approach for detecting ASJs is described. With regard to junction matching, we design a dissimilarity measure in Sec. 4 for use in finding correspondences. The experimental results of our approach are presented and analyzed in Sec. 5. Finally, we conclude our paper in Sec. 6.

1 Related Work

In this section, we briefly review the existing approaches to junction detection and matching as well as geometric structure matching for indoor images.

1.1 Junction Detection

The detection of junction structures in images has been studied for many years [24, 26, 27, 31–34]. Early on, junctions were treated as corner points [31, 32]. For improved recognition, the scales of junctions or other key-points have also been studied [10, 28, 33]. In these approaches, the scales around junction locations are estimated using scale-space theories [9, 10, 33, 35] to handle the changes in viewpoint among different images. Since these approaches determine the scales of the points of interest only in very local areas, they lack high precision and discriminability. Moreover, these methods mainly focus on the locations and scales of corner points while ignoring the differences between different types of junctions.

To overcome these shortcomings, the ACJ detector [28] was proposed for the detection and characterization of junctions using a non-linear scale space. In this work, an *a contrario* approach was proposed for determining the locations and branches of junctions with interpretable isotropic scales, thereby explicitly characterizing ray segments as junction branches and locations. The scale of a detected junction corresponds to the optimal size at which one can observe the junction in the image.

Similar to junction detection, there is an elegant detector named the edge-based region (EBR) detector [12] for detecting affine-invariant regions by estimating the relative speeds at which two points move away from a corner in both directions along curved edges. This work can be regarded as a kind of junction detector for curve-dominated images. However, the straight edges that are common in indoor scenarios cannot be addressed in this way.

Although the approaches introduced above can be used to extract junctions, the geometric representations of those junctions are not sufficiently exploited. The scales estimated using these methods are local and are insufficient for characterizing indoor scenes.

1.2 Junction Matching

Junction matching has received considerable attention since the early years and shows promising matching accuracy [18, 36].

In [18], a model for estimating the endpoints of junction branches was proposed that is very similar to our work in that it estimates an anisotropic scale for each branch. By contrast, however, their approach [18] requires a roughly estimated fundamental matrix, whereas our proposed method estimates the anisotropic scale of each branch directly without requiring a fundamental matrix. When the fundamental matrix is

known, the local homography between a pair of junctions can be estimated to obtain more accurate results and to refine the epipolar geometry [36]. These results are closely related to a recent approach for hierarchical line segment matching based on line-junction-line (LJL) structures [15]. In that work, as a first step, the detected line segments are used to generate junctions with virtual intersections. Then, those junctions are treated as key-points for initial matching. Finally, the epipolar geometry induced by the initial matching is used to estimate the correspondences of the line segments with local junctions. The matching accuracy relies on the descriptors of the virtual intersections. Although the matching results are promising, a better method is needed to solve the problem of estimating the epipolar geometry.

1.3 Indoor Image Matching Based on Geometric Structures

Most indoor scenes can be described using simple geometric elements such as points and line segments. As combinations of points and lines, junctions are also a useful type of geometric structure for describing indoor scenes. Many approaches have been developed for extracting line segments, such as the Canny edge detector [37] and the line segment detector (LSD) [16, 17]. The LSD, which can produce more complete line segments than the Canny edge detector without requiring a parameter tuning procedure, has been applied in many tasks, such as line segment matching [15] and 3D reconstruction [38]. Compared with key-points, line segments can produce more complete results in generating a basic sketch of a scene.

Most algorithms for line segment matching rely on key-point correspondences. More precisely, the key-points in an input image pair are first detected using the SIFT detector [10] or some other detector, whereas the epipolar geometry between the image pair is estimated using RANSAC [39] or one of its variants. Based on the fundamental matrix F induced by the key-point matching, many approaches, such as the line-point-invariant (LPI) approach [14] and the LJL approach [15], have been proposed that can be used to correctly match line segments. The LPI approach has the ability to handle the relations between line segments and matched key-points under changes in viewpoint. In the LJL method [15], image pairs are matched in multiple stages. Although these approaches exhibit good performance in many cases, the matching results tend to show better matching of lines than of line segments. The lines are matched, but the endpoints of the line segments are often not matched very well. In addition to the fact that the estimated epipolar geometry is sometimes erroneous, another important reason for the failure of line segment matching is that line segment detectors cannot guarantee that the line segments they extract will be consistent across varying imaging conditions. In many situations, a line segment l_A that is detected in image I_A might be decomposed into two or more collinear line segments $l_B^1, \ldots, l_B^k$ in another image I_B. In such a case, a line matching result could be regarded as correct if the line l_A were found to correspond to $l_B^1, \ldots, l_B^k$. However, in a typical approach to line segment matching, it will be considered that no correct line segment corresponding to l_A exists in image I_B. Moreover, the existing line segment matchers rely on the results of key-point matching. When key-point matching fails or is inaccurate, the line segment matching result will therefore be affected to some extent.

2 Problem Statement

2.1 Junction Model

Early research on junction detection typically focused on the orientations of the branches and the junction locations while ignoring the length of each branch [24, 26, 27, 31–34]. Although the junction locations and the orientations of the branches are important for representing the geometric structures in indoor images, neglecting the length of the branches limits the achievable indoor image matching performance. Ideally, if the endpoint of junctions can be estimated accurately, the richer structural information will be more helpful for matching indoor images than local features. Motivated by this fact, we propose a new junction model for better characterizing junctions. We define our junction model by considering the endpoint of each branch in a discrete gray-scale image $I : \Omega \mapsto \mathbb{R}$ defined on an image grid $\Omega = \{0, 1, \ldots, n_1 - 1\} \times \{0, 1, \ldots, n_2 - 1\}$, where $n_1 - by - n_2$ is size of the image. Since the length of each branch can be different, we call our model as

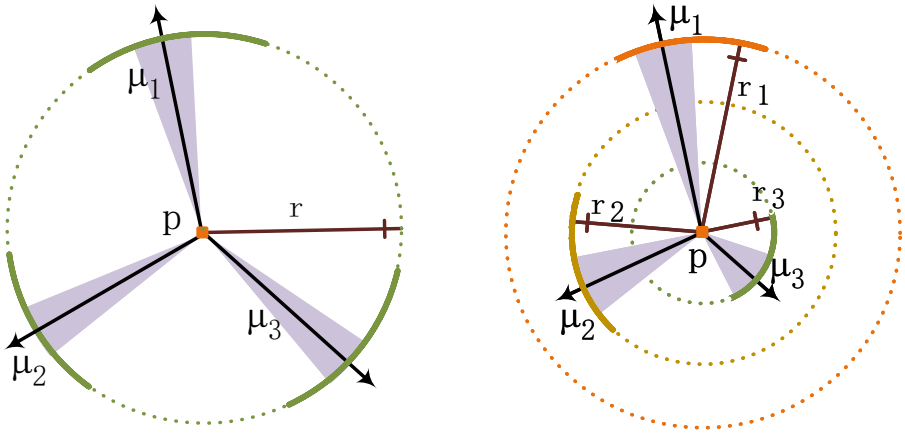

Figure 2: Templates of an isotropic-scale junction (left) as defined by the ACJ detector [28] and an anisotropic-scale junction (ASJ) (right) as proposed in our work.

anisotropic-scale junction model. As a special case of this model, a junction model with isometric branches is an *isotropic-scale junction*.

Definition 1 (Anisotropic-scale junction (ASJ)) *An ASJ with M branches starting at the same point $\boldsymbol{p} \in \Omega$ is denoted by*

$$\jmath = \left\{ \boldsymbol{p}, \{r_i, \theta_i\}_{i=1}^{M} \right\}, \tag{1}$$

where r_i and θ_i are the scale and orientation, respectively, of the i-th branch and M is the number of branches.

Fig. 2 provides an example of the difference between an ASJ (left) and an isotropic-scale junction (right). An *isotropic-scale junction* is actually a special case of the anisotropic model in which the lengths of all branches are identical.

2.2 Detecting Junction Locations and Isotropic Branches

Once the isotropic-scale junction model has been defined, junction detection becomes a template matching problem. Based on this idea, Xia *et al.* exploited the junction-ness of branches with a given scale r and orientations θ_i to derive an *a contrario* approach for extracting meaningful junctions in input images [28]. The junction-ness for a given scale r and orientation θ_i comprises the neighbor information of the normalized gradient. Rather than consisting of points, the neighborhood for a given r and θ_i is a sector. On the left-hand side of Fig. 2, the dark area labeled as θ_1 represents the neighboring sector of the corresponding branch. The neighboring sector for a given location $\boldsymbol{p} \in \Omega$, scale r and orientation θ can be expressed mathematically as

$$\begin{aligned} S_{\boldsymbol{p}}(r, \theta) := \{ \boldsymbol{q} \in \Omega;\ \boldsymbol{q} \neq \boldsymbol{p}, \|\vec{\boldsymbol{pq}}\| \leq r, \\ d_{2\pi}(\alpha(\vec{\boldsymbol{pq}}), \theta) \leq \Delta(r) \}, \end{aligned} \tag{2}$$

where $\Delta(r)$ is defined as $\frac{\tau}{r}$, with τ being some predefined parameter, and Ω is the domain of the input image.

Since a junction is formed of edges and a corner point, the normal angle for the gradient should be consistent with the orientations of the branches. Following this idea, if most points $\boldsymbol{q} \in S_{\boldsymbol{p}}(r, \theta)$ have close normal angles with respect to the orientation θ, then the corresponding scale r and orientation θ should be meaningful as a branch of the junction. For a given sector $S_{\boldsymbol{p}}(r, \theta)$, the junction-ness can be measured as

$$\omega_{\boldsymbol{p}}(r, \theta) = \sum_{\boldsymbol{q} \in S_{\boldsymbol{p}}(r,\theta)} \gamma_{\boldsymbol{p}}(\boldsymbol{q}), \tag{3}$$

where $\gamma_{\boldsymbol{p}}(\boldsymbol{q})$ is the pairwise junction-ness, expressed as

$$\gamma_{\boldsymbol{p}}(\boldsymbol{q}) = \left\|\nabla\tilde{I}(\boldsymbol{q})\right\| \cdot \max(|\cos(\phi(\boldsymbol{q}) - \alpha(\vec{\boldsymbol{pq}}))| - |\sin(\phi(\boldsymbol{q}) - \alpha(\vec{\boldsymbol{pq}}))|, 0) \tag{4}$$

Here, $\left\|\nabla\tilde{I}(\boldsymbol{q})\right\|$ is the norm of the normalized gradient of the image I at point $\boldsymbol{p} \in \Omega$, $\phi(\boldsymbol{q})$ for pixel $\boldsymbol{q}$ is defined as $\phi(\boldsymbol{q}) = (\arctan\frac{I_y(\boldsymbol{q})}{I_x(\boldsymbol{q})} + \pi/2)$ *modulo* (2π), and I_x and I_y are the partial derivatives of the input image I in the x and y directions, respectively.

For an isotropic-scale junction with two or more branches, the minimum junction-ness among the branches is used to describe the junction-ness of the entire junction, as expressed in Eq. (5):

$$t(\jmath) := \min_{m=1,\ldots,M} \omega_{\boldsymbol{p}}(r, \theta_m), \tag{5}$$

where M and m represent the total number of branches and the branch index, respectively, for junction $\jmath$.

2.3 Estimating Anisotropic-Scale Branches

Although Eq. (5) measures the junction-ness of a given junction, it does not contain any information on the anisotropic scales of the branches. This definition of junction-ness includes only the information that each branch's scale r_i is larger than r, and it cannot be used for handling more sophisticated transformations, such as affine transformations and projective transformations. To overcome this problem, we define an ASJ with independent branch scales in Def. 1. The difference between an isotropic-scale junction and an ASJ can be observed in Fig. 2. It is easy to see that the junction-ness of an entire junction as defined in Eq. (5) cannot be used to consider independent scales r_i. Fortunately, however, the isotropic-scale junctions detected by the ACJ detector [28] are meaningful, and the problem of estimating the scale r_i and orientation θ_i can be simplified to the estimation of only the scale r_i for a given location $\boldsymbol{p}$ and orientation θ_i. In other words, once isotropic junctions have been detected, we need a robust method for estimating the length of a corresponding ray segment with a specific orientation θ.

One plausible way to model this unknown scale with respect to a given location $\boldsymbol{p}$ and orientation θ is to simply modify the junction-ness defined in Eq. (3) to $\omega_{\boldsymbol{p}}(r)$ for a specific θ. Then, the *a contrario* approach presented in [28] seems to be a feasible means of checking whether the scale r is ε-meaningful. The corresponding cumulative distribution function (C.D.F.) to be used to obtain an ε-meaningful scale r can be formulated as

$$F(t; J(r,\theta)) = \mathbb{P}\{\omega_{\boldsymbol{p}} \geq t\} = \int_t^{+\infty} d\left(\overset{J(r,\theta)}{\underset{j=1}{\star}} p\right), \tag{6}$$

where p represents the distribution of the random variable $\omega_{\boldsymbol{p}}(r,\theta)$ and is expressed as

$$p(z) = \frac{1}{2}(\delta_0(z) + \frac{2}{\sqrt{\pi}} e^{-\frac{z^2}{4}} \operatorname{erfc}(\frac{z}{2}))\mathbf{1}_{z\geq 0}, \tag{7}$$

$J(r,\theta)$ is the number of pixels in the corresponding neighboring sector, and the operator $\overset{J(r,\theta)}{\underset{j=1}{\star}}$ produces the corresponding $J(r,\theta)$ instances of the convolutional probability density function (P.D.F.), which actually represents the random variable $\omega_{\boldsymbol{p}}(r,\theta)$. The ε-meaningful scale for a given orientation and location can thus be determined from the inequality

$$\mathrm{NFA}(\jmath) := \#\mathcal{J}(1) \cdot F(t; J(r,\theta)) \leq \varepsilon, \tag{8}$$

where $\#\mathcal{J}(1)$ is the number of tests for a junction with 1 branch.

However, for the number of false alarms (NFA) defined in Eq. (8), it must be considered that indoor images often contain several junctions with extremely large-scale branches. This fact can invalidate the above

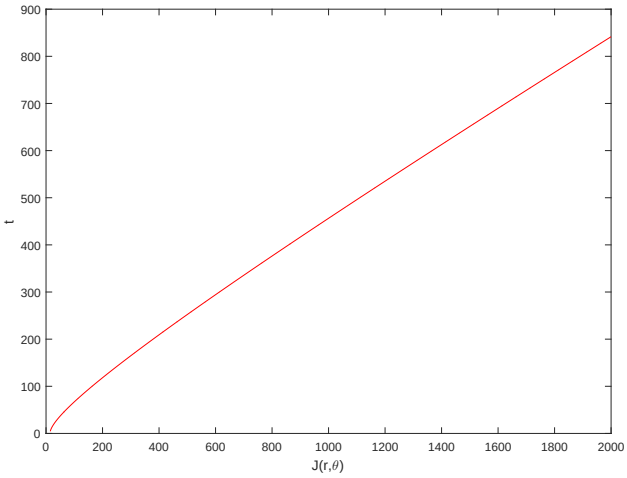

Figure 3: The relationship between the number of convolutions $J(r,\theta)$ and the corresponding minimal junction-ness such that $F(t;J(r,\theta))=0$.

inequality. To illustrate this problem, let us consider the relationship between the number of convolutions $J(r,\theta)$ and the minimal junction-ness for which the probability $F(t;J(r,\theta))$ is equal to 0. As shown in Fig. 3, if the value of $\omega_{\boldsymbol{p}}(r,\theta)$ is greater than $\frac{J(r,\theta)}{2}$, then the probability $F(t;J(r,\theta))$ will always be equal to 0, which may cause the inequality to degenerate to $0\leq\varepsilon$. In fact, the pairwise junction-ness defined in Eq. (4) can reach 1, in which case $\omega_{\boldsymbol{p}}(r,\theta)$ will be equal to $J(r,\theta)$. Therefore, the junction-ness proposed in [28] is unfeasible for modeling the unknown scale of a branch.

3 An *A Contrario* Model for ASJ Detection

To solve the problems introduced in Sec. 2, we derive a differential junction-ness model for depicting the scale for a given location and orientation. Since the scale r_i of each branch of junction $\jmath$ is independent of the scale of each other branch, we simply model the endpoint of each branch independently.

3.1 Differential Junction-ness Model

Suppose that isotropic junctions have been detected using a small scale r_0; then, the inherent scales of the branches will be greater than r_0. If we increase the scale r_0 to a larger value r_1, although the junction-ness will be larger, the error $\omega_{err}=\omega_{\boldsymbol{p}}(r_1,\theta)-\omega_{\boldsymbol{p}}(r_1,\theta)$ will not be significantly increased. A reasonable way to recognize this insignificant variation is to study the variation of $\omega_{\boldsymbol{p}}(r,\theta)$ with respect to an increased r. Here, we first reformulate the junction-ness of a branch, as expressed in Eq. (3), in a continuous form. The junction-ness for a position $\boldsymbol{p}$, scale R and orientation θ is

$$\omega_{\boldsymbol{p}}(r,\theta)=\int_0^r dr\int_{\theta-\delta(r)}^{\theta+\delta(r)}\gamma_{\boldsymbol{p}}\left(\boldsymbol{p}+r\left(\cos\psi,\sin\psi\right)\right)d\psi, \tag{9}$$

where $\delta(r)$ is the angle width for a given scale; here, we select $\delta(r)=\frac{\tau}{r}$. The discrete partial derivative $\frac{\partial\omega_{\boldsymbol{p}}(r,\theta)}{\partial r}$ is given by

$$\begin{aligned}\frac{\partial \omega_{\boldsymbol{p}}(r,\theta)}{\partial r} &= \sum_i \gamma_{\boldsymbol{p}}\left(\boldsymbol{p} + r\begin{bmatrix}\cos\psi_i\\ \sin\psi_i\end{bmatrix}\right)\\ &+\delta'(r)\sum_i \gamma_{\boldsymbol{p}}\left(\boldsymbol{p} + r_i\begin{bmatrix}\cos(\theta-\delta(r))\\ \sin(\theta-\delta(r))\end{bmatrix}\right)\\ &+\delta'(r)\sum_i \gamma_{\boldsymbol{p}}\left(\boldsymbol{p} + r_i\begin{bmatrix}\cos(\theta+\delta(r))\\ \sin(\theta+\delta(r))\end{bmatrix}\right),\end{aligned} \tag{10}$$

where ψ_i is the i-th sample angle in the range $[\theta-\delta(r), \theta+\delta(r)]$ and r_i is the i-th sample point in the range $[0, r]$.

3.2 Null Hypothesis and Distribution

After building the differential junction-ness model, we need to find a robust way to check whether the value of $\partial\omega_{\boldsymbol{p}(r,\theta)}/\partial r$ for a specific r is sufficiently significant. One way to achieve this goal is to develop an *a contrario* approach for automatically controlling the threshold. Since our work is an extension of the ACJ detector [28], the null hypothesis here should be the same; we say that the variables $\left\|\nabla\tilde{I}(\boldsymbol{q})\right\|$ and $\phi(\boldsymbol{q})$ satisfy the null hypothesis $\mathcal{H}_0$ if

1. $\forall \boldsymbol{q}\in\Omega$, $\left\|\nabla\tilde{I}(\boldsymbol{q})\right\|$ follows a Rayleigh distribution with parameter 1;
2. $\forall \boldsymbol{q}\in\Omega$, $\phi(\boldsymbol{q})$ follows a uniform distribution over $[0, 2\pi]$; and
3. all of the random variables $\left\|\nabla\tilde{I}(\boldsymbol{q})\right\|$ and $\phi(\boldsymbol{q})\}_{\boldsymbol{q}\in\Omega}$ are independent of each other.

According to the discussion presented in [28], every $\gamma_{\boldsymbol{p}}(\boldsymbol{q})$ independently follows the distribution given in Eq. (7). The random variable $\frac{\partial\omega_{\boldsymbol{p}(r,\theta)}}{\partial r}$ follows the distribution of the random variable

$$S_r = \sum_{i=1}^{m} X_i + \delta'(r)\sum_{i=1}^{k}(Y_i + Z_i), \tag{11}$$

where the random variables X_i, Y_i, and Z_i follow the distribution given in Eq. (7); m is the number of sampling points for ψ_i; and k is the number of sampling points for r_i. The function $\delta'(r)$ will be very small for reasonable values of r (for example, $r \geq 4$ induces $|\delta'(r)| = \frac{\tau}{r^2} \leq \frac{\tau}{16}$) because the parameter τ should have small values. Hence, this random variable can be approximated as $S_r \approx \sum_{i=1}^{m} X_i$ for computational simplicity. In practice, k will be larger than 10, and therefore, the P.D.F. of $\sum_{i=1}^{k}(Y_i + Z_i)$ can be accurately approximated using the Central Limit Theorem (CLT) as follows:

$$f(t) = \frac{1}{\sqrt{4k\sigma^2\pi}}\exp\left(-\frac{(t-2k\mu)^2}{4k\sigma^2}\right), \tag{12}$$

where μ and σ^2 are the expectation value and variance, respectively, of (7). The P.D.F. of $\delta'(R)\left(\sum_{i=1}^{k} Y_i + Z_i\right)$ is

$$\tilde{f}(t) = \frac{R^2}{\tau}f(-\frac{R^2}{\tau}t) = \frac{1}{\sqrt{2\pi\cdot 2k\sigma^2\frac{\tau^2}{R^4}}}\exp\left(-\frac{t+\frac{2\tau}{R^2}k\mu}{2\cdot 2k\sigma^2\frac{\tau^2}{R^4}}\right), \tag{13}$$

which is the Gaussian distribution with a mean of $-\frac{2\tau}{R^2}k\mu$ and a variance of $2k\sigma^2\tau^2/R^4$. Meanwhile, the random variable $\sum_{i=1}^{m} X_i$ follows $\mathcal{N}(m\mu, m\sigma^2)$. Therefore, the random variable S approximately follows the distribution $\mathcal{N}(m\mu - 2k\mu\frac{\tau}{R^2}, m\sigma^2 + 2k\sigma^2\tau^2/R^4)$.

The probability $\mathbb{P}\left(S_r \geq \frac{\partial \omega_{\boldsymbol{p}}(r,\theta)}{\partial r}\right)$ for a given r and θ follows the distribution $f(t)$:

$$\mathbb{P}_{\boldsymbol{p}}(r,\theta) := \mathbb{P}\left(S_r \geq \frac{\partial \omega_{\boldsymbol{p}}}{\partial r}\right) = \int_{\partial \omega_{\boldsymbol{p}}/\partial r}^{\infty} d\left(\overset{M}{\underset{i=1}{\star}} p\right), \tag{14}$$

which indicates that the scale cannot be increased by a sufficiently small increment in R along orientation θ under hypothesis $\mathcal{H}_0$. The smaller the probability $\mathbb{P}_{\boldsymbol{p}}(r,\theta)$ is, the more confident we can be that the scale r is a reasonable scale. A small probability $\mathbb{P}(r,\theta)$ means that the point $\boldsymbol{p} + r \cdot [\cos\theta, \sin\theta]$ has a high possibility of belonging to the branch. Ideally, an existing branch should produce a series of small probabilities in an interval $[r_0, r_1]$. Then, the (maximum) scale of the branch should be defined as r_1. We use the probability $\mathbb{P}_{\boldsymbol{p}}(r,\theta)$ to check whether the point $\boldsymbol{p}_r^{\theta} = \boldsymbol{p} + r \cdot [\cos\theta, \sin\theta]^T$ belongs to the branch.

3.3 Number of Tests and Number of False Alarms

In the previous subsection, we concluded that a *sufficiently* small probability $\mathbb{P}_{\boldsymbol{p}}(r,\theta)$ indicates that the corresponding point with a certain direction θ and radius R has a high probability of belonging to the branch. However, the definition of this *sufficient* probability needs to be clarified. According to the Helmholtz principle, we bound the *sufficient* probability by stating that the expected number of occurrences of this event should be less than ε under the *a contrario* random assumption [40] as follows:

$$\mathrm{NFA}(r, \boldsymbol{p}, \theta) = N_s \cdot \mathbb{P}_{\boldsymbol{p}}(r,\theta) \leq \varepsilon,$$

where N_s denotes the number of occurrences of points along the given location and orientation. Since the location and orientation of the branch are known, the expected NFA should be smaller than $\sqrt{NM}$, where N and M are the numbers of rows and columns, respectively, in the corresponding image. When the hypothesis H_0 is rejected for the point $\boldsymbol{p}_r^{\theta}$ $\forall r \in (0, r_1]$, the scale of the branch should be r_1. The scale R is called the maximum (meaningful) scale of the branch if R is the maximum scale that satisfies the inequality

$$\mathrm{NFA}(r, \boldsymbol{p}, \theta) = \sqrt{NM} \cdot \mathbb{P}_{\boldsymbol{p}}(r,\theta) \leq \varepsilon, \forall r \in (0, R].$$

Usually, the value of ε is defined as 1, which means that the expected NFA is no larger than 1.

3.4 Scale Ambiguity for Branches

Junctions are located at the intersections of line segments. Suppose that there exist two junctions $\jmath_1 = \{\boldsymbol{p}_1, \{r_1^1, \theta_1^1\}, \{r_1^2, \theta_1^2\}\}$ and $\jmath_2 = \{\boldsymbol{p}_2, \{r_2^1, \theta_2^1\}, \{r_2^2, \theta_2^2\}\}$, where the two-tuple $\{\{r_i^j, \theta_i^j\}\}$ denotes the scale and orientation of the j-th branch of the i-th junction and $\boldsymbol{p}_i$ is the location of the i-th junction. In the case that junction $\jmath_2$ is located at $\boldsymbol{p}_2 = \boldsymbol{p}_1 + r_1^1 \left[\cos\theta_1^1, \sin\theta_1^1\right]^T$ and $\theta_1^1 = \theta_2^1$, scale ambiguity occurs because the line segment $\boldsymbol{p}_1\boldsymbol{p}_2$ and the branch $\{r_2^1, \theta_2^1\}$ are collinear. The scale of the first branch of $\jmath_1$ could be regarded as either r_1^1 or $r_1^1 + r_2^1$. For example, there are two junctions $\jmath_1$ and $\jmath_2$ located at $\boldsymbol{p}_1$ and $\boldsymbol{p}_2$, respectively, in Fig. 4. The branches that lie along the direction of $\boldsymbol{p}_1\boldsymbol{p}_2$ for $\jmath_1$ and $\jmath_2$ are collinear with the line segment marked in red. For the relevant branch of $\jmath_1$, its scale may be $\|\boldsymbol{p}_2 - \boldsymbol{p}_1\|$, $\|\boldsymbol{p}_3 - \boldsymbol{p}_1\|$ or $\|\boldsymbol{p}_4 - \boldsymbol{p}_1\|$, whereas the scale of the relevant branch of $\jmath_2$ may be $\|\boldsymbol{p}_3 - \boldsymbol{p}_2\|$ or $\|\boldsymbol{p}_4 - \boldsymbol{p}_2\|$. To eliminate the ambiguity, we define the scale of a branch as follows.

Definition 2 (Scale of a branch) *Suppose that there exists a branch starting at point $\boldsymbol{p}$ in direction θ and that the possible salient scales are $r_1, r_2, \ldots, r_m$. We define the scale of this branch, r^*, as*

$$r^* = \max_i r_i.$$

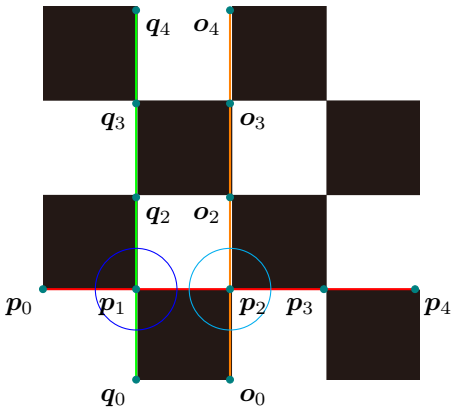

Figure 4: Scale ambiguity for branches. The junctions $\jmath_1$ and $\jmath_2$, located at $\boldsymbol{p}_1$ and $\boldsymbol{p}_2$, respectively, have more than one possible scale.

A branch with such a scale is more stable and more global than other features. However, several challenges are encountered in estimating such scales from images. Most existing approaches and the model proposed in Sec. 3.3 estimate line segments or branches based on the orientations of level lines extracted from the gradient of the input image [16]. The line segment detected from the image in Fig. 4 could be either $\boldsymbol{p}_1\boldsymbol{p}_2$ or $\boldsymbol{p}_1\boldsymbol{p}_3$ because the level line near the point $\boldsymbol{p}_2$ will most probably be aligned with the orientation of the vector $\boldsymbol{o}_2 - \boldsymbol{p}_2$, which will lead to line segments that are collinear with the branch of $\jmath_1$ that crosses from point $\boldsymbol{p}_2$ to $\boldsymbol{p}_3$ or $\boldsymbol{p}_4$. When the viewpoint changes, the illumination varies or the noise increases, the orientations of the level lines near $\boldsymbol{p_2}$, $\boldsymbol{p}_3$ and $\boldsymbol{p}_4$ will also shift in accordance with their uncertainty. Therefore, the scale cannot be robustly estimated under different imaging conditions.

Fortunately, the inherent property of the location of a junction is stable regardless of the imaging conditions. Although the orientations of the level lines around the location of a junction are subject to uncertainty, most of them will still be aligned with one of the lines that intersects the junction. Motivated by this fact, we use highly local isotropic-scale junctions with a small neighborhood size (e.g., a 5×5 or 7×7 window size) instead of the gradient field and level lines. For a given pixel in an image, we calculate the junction-ness for different orientations in a small neighborhood in accordance with the ACJ algorithm [28] as follows:

$$\omega_{\boldsymbol{p}}(\theta) = \frac{1}{\sigma}\left(\sum_{\boldsymbol{q}\in S_{\boldsymbol{p}}(\theta)} \frac{\gamma_{\boldsymbol{p}}(\boldsymbol{q})}{\sqrt{n}} - \sqrt{n}\mu\right), \tag{15}$$

where $S_{\boldsymbol{p}}(\theta)$ is defined in Eq. (2) for a fixed radius (e.g., $r = 3, 5, 7$), n is the cardinal number of the set $S_{\boldsymbol{p}}(\theta)$, and μ and σ^2 are the mean and variance, respectively, that are defined in Eq. (13). Then, we leverage non-maximal suppression (NMS) [41] to obtain the highly local junctions and filter out branches for these junctions with non-meaningful NFA values according to Eq. (8). These highly local junctions are denoted by $\jmath_{\boldsymbol{p}} = \{\theta^i_{\boldsymbol{p}}, \omega^i_{\boldsymbol{p}}, \mathrm{NFA}^i_{\boldsymbol{p}}\}_{i=1}^K$, where $\omega^i_{\boldsymbol{p}}$ and $\mathrm{NFA}^i_{\boldsymbol{p}}$ are the strength and corresponding NFA value, respectively, for the branch with orientation θ_i. In the case that pixel $\boldsymbol{p}$ is on (near) an edge, there will be two θ_i values that align with the orientation of this edge up to $\pm\pi$. If pixel $\boldsymbol{p}$ is near another junction, then there will be multiple orientations aligned with different branches of this junction. Meanwhile, we incorporate the strength $\omega^i_{\boldsymbol{p}}$, instead of the norm of the (normalized) gradient, into the *a contrario* model proposed in Sec. 3.3 with a modified probability distribution.

3.5 Modified Probability Distribution

For estimating the scale of a branch using the definition given in Eq. 2, the functions $\gamma_{\boldsymbol{p}}$ and $\omega_{\boldsymbol{p}}(r,\theta)$ for measuring the junction-ness should be changed to

$$\begin{aligned}\tilde{\gamma}_{\boldsymbol{p}}(\boldsymbol{q}) = \omega^i_{\boldsymbol{q}} \cdot \max(&\left|\cos(\theta^i_{\boldsymbol{q}} - \alpha(\vec{\boldsymbol{pq}}))\right| - \\ &\left|\sin(\theta^i_{\boldsymbol{q}} - \alpha(\vec{\boldsymbol{pq}}))\right|, 0)\end{aligned} \tag{16}$$

and

$$\tilde{\omega}_{\boldsymbol{p}}(r,\theta) = \sum_{\boldsymbol{q}\in S_{\boldsymbol{p}}(r,\theta)} \tilde{\gamma}_{\boldsymbol{p}}(\boldsymbol{q}), \tag{17}$$

where the index i in Eq. (16) indicates the orientation $\theta^i_{\boldsymbol{q}}$ that is closest to θ.

According to the CLT, the random variable $\omega^i_{\boldsymbol{p}}$ follows a Gaussian distribution with a mean of 0 and a variance of 1, and the distribution of $\tilde{\gamma}_{\boldsymbol{p}}(\boldsymbol{q})$ is

$$\tilde{p}(z) = \frac{1}{2}\delta_0(z) + \mathbf{1}_{z\neq 0}\frac{\sqrt{2}}{\sqrt{\pi^3}}\int_0^1 \frac{1}{y} e^{-\frac{z^2}{2y^2}} \frac{1}{\sqrt{2-y^2}} dy. \tag{18}$$

Thus, the null hypothesis discussed in Sec. 3.2 should be updated to

$$\mathbb{P}_{\boldsymbol{p}}(r,\theta) := \mathbb{P}\left(S_r \geq \frac{\partial\tilde{\omega}_{\boldsymbol{p}}}{\partial r}\right) = \int_{\partial\tilde{\omega}_{\boldsymbol{p}}/\partial r}^{\infty} d\left(\overset{M}{\underset{i=1}{\star}}\tilde{p}\right). \tag{19}$$

3.6 Junction Detection

Thus far, the *a contrario* approach for anisotropic scale estimation has been derived. For an input image, isotropic junctions and local junctions for each pixel are first detected using the ACJ detector [28] for initialization. The isotropic junction results are denoted by $\{\jmath_i\}_{i=1}^N$, and the local junctions at a fixed small scale (usually $r = 3, 5, 7$) for every pixel are $\jmath_{\boldsymbol{p}} = \{\theta^i_{\boldsymbol{p}}, \omega^i_{\boldsymbol{p}}, \mathrm{NFA}^i_{\boldsymbol{p}}\}_{i=1}^K$, where $\boldsymbol{p}$ represents the pixel coordinates.

We estimate the scale r^j_i of branch θ^j_i based on the NFA:

$$\mathrm{NFA}(r^j_i, \boldsymbol{p}_i, \theta^j_i) = \sqrt{NM}\cdot\mathbb{P}_{\boldsymbol{p}}(r^j_i, \theta^j_i) \leq \varepsilon,$$

where the probability $\mathbb{P}_{\boldsymbol{p}}(r,\theta)$ is the updated version given in Eq. (19). The scale r^j_i is sought, starting at r_i, until the NFA is larger than ε.

The accuracy of the orientations of the branches detected by the ACJ detector [28] depends on the scale r_i, which is bounded by a predefined parameter and hence is noisy. The ASJ scales are sensitive to this noise and should be refined. The branch with the most accurate orientation θ should have the maximum junction-ness with the scale r_θ; thus, we optimize the objective function

$$\hat{\theta} = \arg\max_{\theta} \sum_{\boldsymbol{q}\in S_{\boldsymbol{p}}(r_\theta,\theta)} \gamma_{\boldsymbol{p}}(\boldsymbol{q}) \tag{20}$$

to refine the orientation θ and check that the branch with orientation $\hat{\theta}$ and scale $r_{\hat{\theta}}$ is an ε-meaningful branch.

4 ASJ Matching for Indoor Images

Since ASJs contain rich structural information as represented by their anisotropic scales, in this section, we study a matching method that can take full advantage of ASJs. For a pair of junctions $\jmath^P$ and $\jmath^Q$ detected

from images I^P and I^Q, respectively, a homography can be estimated from the point set that contains their locations and the endpoints of their branches, which can be used to compare junctions to identify correct correspondences. Since various types of junctions (L-junctions, Y-junctions and X-junctions) may exist in an image and the type of a given junction might differ across images because of occlusion, the homography estimated from a pair of junctions might be invalid. Fortunately, regardless of the junction type, the location can be obtained from the intersection of any two branches that are not parallel to each other, which means that a junction with more than two branches can be decomposed into multiple L-junctions. Moreover, any L-junction with two branches whose orientations θ^1 and θ^2 are equal up to π should be filtered out. After such decomposition and filtering, all junctions detected in an image will be L-junctions.

The perspective effects in a local patch are typically small [42] and can be approximated via an affine homography. We use pairs of L-junctions to estimate such homographies. Suppose that there are N^P and N^Q decomposed L-junctions in images I^P and I^Q, denoted by $\{\jmath_i^P\}_{i=1}^{N^P}$ and $\{\jmath_i^Q\}_{i=1}^{N^Q}$, respectively. If a pair of junctions $(\jmath_n^P, \jmath_m^Q)$ are matched, then an affine homography can be deduced once the orientations have been determined. To derive a unique affine homography, we define the partial order for the two branches (r^1, θ^1) and (r^2, θ^2) of an L-junction as

$$\begin{cases} (r^1, \theta^1) < (r^2, \theta^2), \ \ if \langle \theta^1, \theta^2 \rangle < \pi, \\ (r^1, \theta^1) < (r^2, \theta^2), \ \ if \langle \theta^1, \theta^2 \rangle > \pi. \end{cases} \tag{21}$$

Every junction needs to be sorted in accordance with the order defined above. The affine homography for a pair of junctions $\jmath_n^P$ and $\jmath_m^Q$ is estimated using the Direct Linear Transform (DLT) based on their locations and the endpoints of their branches. More precisely, we solve the equations

$$\boldsymbol{q}_i = H\boldsymbol{p}_i, \ \ i = 0, 1, 2, \tag{22}$$

where $\boldsymbol{p}_i$ and $\boldsymbol{q}_i$ are the homogeneous representations of the locations and two branches of $\jmath_n^P$ and $\jmath_m^Q$, respectively. The matrix H, which is expressed as

$$H = \begin{bmatrix} h_1 & h_2 & h_3 \\ h_4 & h_5 & h_6 \\ 0 & 0 & 1 \end{bmatrix},$$

represents the affine transform induced by $\boldsymbol{p}_i$ and $\boldsymbol{q}_i$ for $i = 0, 1, 2$.

For the image pair (I^P, I^Q), we can obtain $N^P \times N^Q$ affine homographies, denoted by $H_{n,m}$, each of which maps the n-th junction in I^P to the m-th junction in I^Q. For a correct correspondence, the matrix $H_{n,m}$ will accurately map image I^P to image I^Q near the location of the junction, whereas a homography corresponding to a mismatching junction pair will map the image I^P correctly only at the branch endpoints and junction location and erroneously at other positions. To save computational resources, we map only a patch $\mathcal{P}(\jmath_n^P)$ around $\jmath_n^P$ to $\mathcal{P}(\jmath_n^Q)$ in I^Q and map $\mathcal{P}(\jmath_m^Q)$ to $\mathcal{P}(\jmath_m^P)$ in I^P by using the matrix $H_{n,m}$ and its inverse $H_{n,m}^{-1}$. Then, the distance between the two features $\jmath_n^P$ and $\jmath_m^Q$ can be measured as

$$\mathcal{D}(\jmath_n^P, \jmath_m^Q) = \tilde{D}(\mathcal{P}(\jmath_n^P), \mathcal{P}(\jmath_n^Q)) + \tilde{D}(\mathcal{P}(\jmath_m^Q), \mathcal{P}(\jmath_m^P)), \tag{23}$$

where the distance $\tilde{D}$ is the distance between two patches as calculated based on the raw patches, the SIFT descriptors or some other descriptors.

Benefiting from the characteristics of the homographies induced by ASJs, the distance between the original and mapped patches for a correct correspondence is usually very small, whereas it is larger for an incorrect correspondence. Consequently, we can use the ratio test proposed in [10] to filter out incorrect correspondences.

5 Experimental Analysis

This section presents and analyzes the results of the proposed ASJ detection and matching routines in comparison with existing methods of junction detection, junction matching, key-point matching and line segment

Table 1: Average number of false detections in 1000 Gaussian-noise images

ϵ	0.01	0.1	1	10	100	200
Avg. False	0.002	0.006	0.198	5.923	66.472	132.676

correspondence identification. In our experiments, we first detect ASJs using the procedures presented in Section 3 and then identify the correspondences between junctions based on the affine homographies induced by these semi-local geometric structures.

5.1 Stability and Control of the Number of False Detections

The *a contrario* approach detects meaningful events as controlled by a threshold ϵ, which bounds the average number of false detections in an image based on the null hypothesis. In this subsection, we check the average number of false detections in Gaussian-noise images and present the ASJ detection results for a fixed threshold ϵ.

Experimentally, we generate 1000 random images of 256×256 pixels that independently follow a standard Gaussian distribution on a pixel-wise basis. For each pixel, we randomly generate an orientation from a uniform distribution on the interval $[0, 2\pi)$ and estimate the scale at this pixel based on the orientation. Ideally, no meaningful line segment structure will appear in these random images, but such structures might be mistakenly detected; this behavior can be used to count the average number of false detections. If the number of false detections can be controlled by means of the *NFA* as dictated by the proposed *a contrario approach*, then this approach can be characterized as correct. The average numbers of false detections

(a) Original images

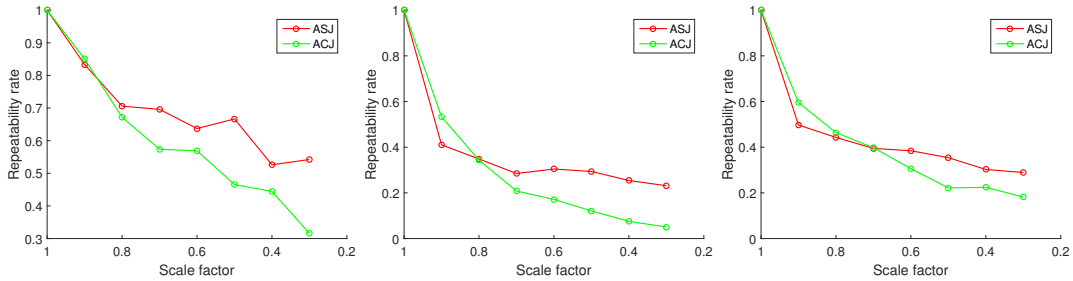

(b) Repeatability with respect to scale changes

Figure 5: Repeatability with respect to scale changes. The original images used to generate the image sequences are shown in the first row. In the second row, the repeatabilities are shown as a function of the scale factor.

in 1000 Gaussian-noise images for various values of the bound ϵ on the NFA value are reported in Tab. 1. The value of ϵ varies in our experiments from 10^{-2} to 10^{2}, and the corresponding average number of false

detections is upper bounded by this value.

5.2 Comparison with the ACJ Detector

It is necessary to compare the repeatability of our proposed ASJ detector with that of the ACJ detector because we extended the *a contrario* model used in the ACJ approach for scale estimation. Following on the baseline experiments proposed in [28], the images are first zoomed by different scale factors to generate image sequences with changes in scale. Then, the ASJ and ACJ detectors are applied to these image sequences for junction detection. The repeatability of the ACJ detector is discussed in [28]; however, the definition of junction correspondence used in that study focuses only on the locations and branches of the junctions while ignoring their scale coherence. Therefore, here, we use a definition of correspondence for the ACJ and ASJ results that considers scale information. For the original image I_0 and the scaled image $I_s = s(I_0)$, corresponding ACJ junctions should have similar locations, branch orientations and branch scales. In addition, two junctions with different numbers of branches cannot be identified as corresponding. More precisely, we define two ACJ junctions $\jmath_1 = \{\boldsymbol{p}_1, r_1, \{\theta_i\}_i = 1^M\}$ and $\jmath_2 = \{\boldsymbol{p}_2, r_2, \{\theta_i^s\}_i = 1^M\}$ detected in I_0 and I_s, respectively, as corresponding if they satisfy

$$\|s \cdot \boldsymbol{p}_1 - \boldsymbol{p}_2\|_2 < 3, \tag{24}$$

$$|s \cdot r_1 - r_2| < 3, \tag{25}$$

$$\max_{\theta \in \{\theta_i\}_i = 1^M} \min_{\theta' \in \{\theta_i\}_i = 1^M} d_{2\pi}(\theta, \theta') < \frac{\pi}{20}, \tag{26}$$

where the angular distance $d_{2\pi}(\theta, \theta') = \min(|\theta - \theta'|, 2\pi - |\theta - \theta'|)$. Similar to the above, the correspondence for two junctions $\jmath_1 = \{\boldsymbol{p}_1, \{r_i, \theta_i\}_i = 1^M\}$ and $\jmath_2 = \{\boldsymbol{p}_2, \{r_i^s, \theta_i\}_i = 1^M\}$ detected using the ASJ approach should satisfy the inequalities expressed in Eq. (24) and Eq. (26) as well as

$$\max_{r \in \{r_i\}_i = 1^M} \min_{r' \in \{r_i^s\}_i = 1^M} |s \cdot r - r'| < 3. \tag{27}$$

In this experiment, the set of scale factors is $\{1.0, 0.9, 0.8, \ldots, 0.3\}$, and the results are shown in Fig. 5. The repeatability curve shows that our proposed ASJ detector performs better than the ACJ detector. The repeatability rate reported in [28] is higher; however, it reflects only the accuracy of the junction locations and branch orientations. In our experiment, the scale coherence is also considered.

As reported in [28], the scale of an ACJ junction represents the length of the shortest branch, and it varies roughly linearly with the scale factor [28]. Theoretically, if a detected ACJ junction has a scale of r in the original image, then the scale of its corresponding junction in the scaled image $s(I)$ should be close to $s \cdot r$. However, an upper bound on the scale is required as an input to the ACJ algorithm, and this bound is recommended to be set in the range of $[12, 30]$ [28] for computational efficiency. In reality, the junctions in indoor images usually have large-scale branches and cannot be reasonably bound by such a relatively small constant.

To demonstrate this fact, we compare several detected junctions in Fig. 6. In this experiment, the junctions are first detected by the ACJ detector in the original image I and the image $s(I)$, which has been scaled by a factor s. Then, we find the corresponding ACJ junctions in the image pair using the inequalities given in Eq. (26) and Eq. (24) while ignoring Eq. (25). For comparison of the scales of the junctions with the factor s, all correspondences are shown as colored circles. In Fig. 6, a correspondence of $\jmath_2 = \boldsymbol{p}_2, r_2, \{\theta_i^s\}_{i=1}^M$ in image $s(I)$, which has a scale of r_1, is shown as a yellow circle with a radius of $r_1 \cdot s$. The red circle and green line segments represent the junction $\jmath_2$. We observe that several correspondences exist that do not have consistent scales. If a junction is formed of several line segments with lengths that are more than $1/s$ times the maximum radius threshold of the ACJ algorithm, then the scale of the junction will be equal to the threshold in the original image. When the image is zoomed by a factor s, the scale of the detected junction

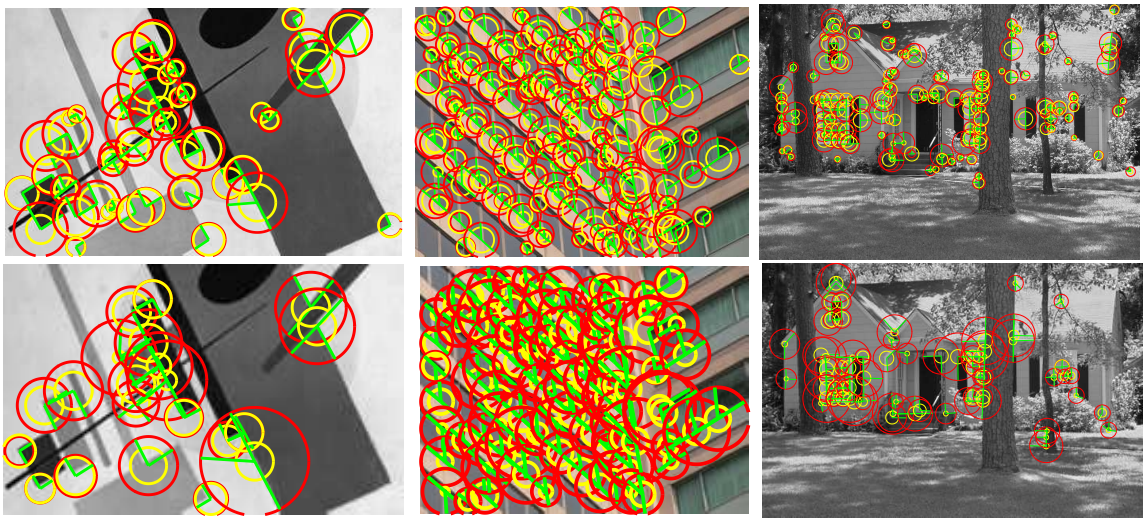

Figure 6: Scale consistency between an original image and a scaled image. The *yellow circles* represent the scales estimated in the images scaled by a factor s, whereas the *red circles* represent the scales detected in the original images. The scale factors are $s = 0.6$ for the top row and $s = 0.3$ for the bottom.

will not decrease because it is still larger than the threshold. This is the reason why the repeatability is lower when we use the inequality defined in Eq. (25) to calculate it.

To conclude this subsection, several example results of the ASJ detector for indoor images are shown in Fig. 7. The ASJ results are shown in the middle column, and the ACJ results are presented in the right column. The results reveal that the ASJ detector has the ability to detect more geometric structures than the ACJ detector. The anisotropic-scale branches of the detected junctions can effectively depict the layout of an indoor scene. By contrast, the ACJ results merely represent highly local information. For example, for several rectangles in Fig. 7, our ASJ detector can produce the boundaries of the rectangles, whereas the ACJ algorithm detects only the corner points and the orientations around the corners.

5.3 ASJ Matching

To evaluate our approach, we collected more than 100 images to which to apply our proposed ASJ detector. Some of the collected images are from the indoor 3D reconstruction datasets presented in [29, 30], whereas we acquired others ourselves. As shown in Fig. 8, the collected images are less textured than natural images. Some of them contain large viewpoint changes and regions with indistinct repeating textures, such as in Fig. 8(b), Fig. 8(i) and Fig. 8(l).

We define two junctions as matching only if the junction centers and branch orientations correspond. In this sense, our matching results extend somewhat beyond the information provided by local features and can be compared with existing approaches from two different perspectives:

- Our method is comparable to key-point matching methods if we regard junctions as specific corner points with two orientations.
- Our method is also comparable to line segment matching methods if we treat junctions as multiple intersecting line segments.

From the key-point matching perspective, we compare the junction matching results with those of the SIFT approach [10], the Affine-SIFT approach [13, 43], the Hessian-Affine approach [44], and the EBR and intensity-based region (IBR) detectors presented in [12].

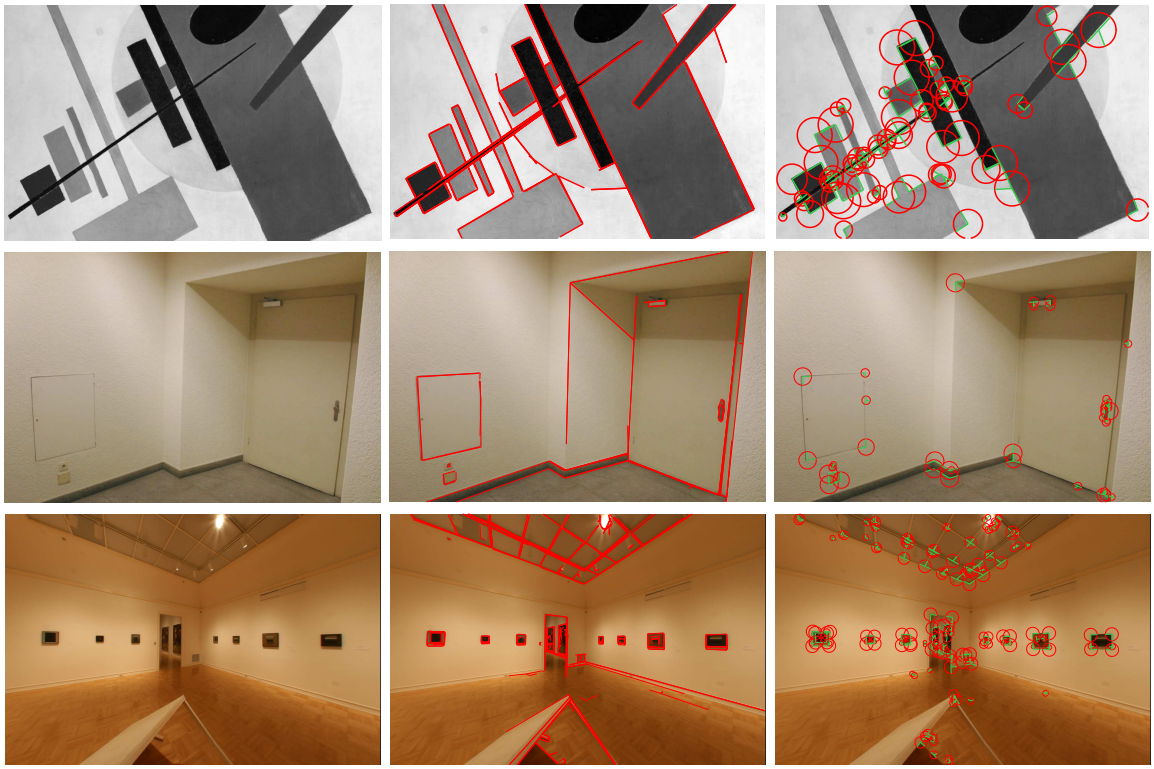

Figure 7: The results of the ASJ detector for the input images shown in the first column are presented in the middle column. The junctions detected by the ACJ detector are shown in the right column for comparison.

Meanwhile, we compare our matching accuracy with those of the existing LPI [14] and LJL [15] approaches for matching line segments, where the proportion of matches is calculated based on whether their endpoints correspond. This is a relatively strict rule for assessing line segment matching results. Interestingly, the LPI [15] and LJL [15] approaches use an epipolar geometry without outliers to assist their line segment matchers, whereas our proposed method, which does not rely on the epipolar geometry, achieves better accuracy.

The implementations of the Affine-SIFT [13,43], Hessian-Affine [44], LPI [14] and LJL [15] methods were obtained from their authors' homepages. The EBR and IBR [12] implementations were obtained from the VGG website[1]. The version of the SIFT detector used here is provided by VLFeat[2]. The descriptor used in our experiment is SIFT, and the mismatches are filtered in accordance with the ratio test with a threshold of 1.5, which is the default threshold for computing matches based on the descriptor in VLFeat, for the ASJ, SIFT [10], Hessian-Affine [44], EBR [12] and IBR [12] detectors by comparing the ℓ_2-distances. Remarkably, the implementation of Affine-SIFT [13, 43] provided by its authors uses a threshold of 1.33 because they calculate the distance using the ℓ_1-norm; in our experiment, we leave this threshold unchanged. However, since the released code for Affine-SIFT [13, 43] produces matched results with outlier filtering, we removed this procedure to ensure fairness; consequently, the results of our experiments differ from those of the released executable. All of the parameters used in the approaches considered for comparison are the default values provided by their authors.

[1] http://www.robots.ox.ac.uk/~vgg/research/affine/descriptors.html#binaries
[2] http://www.vlfeat.org

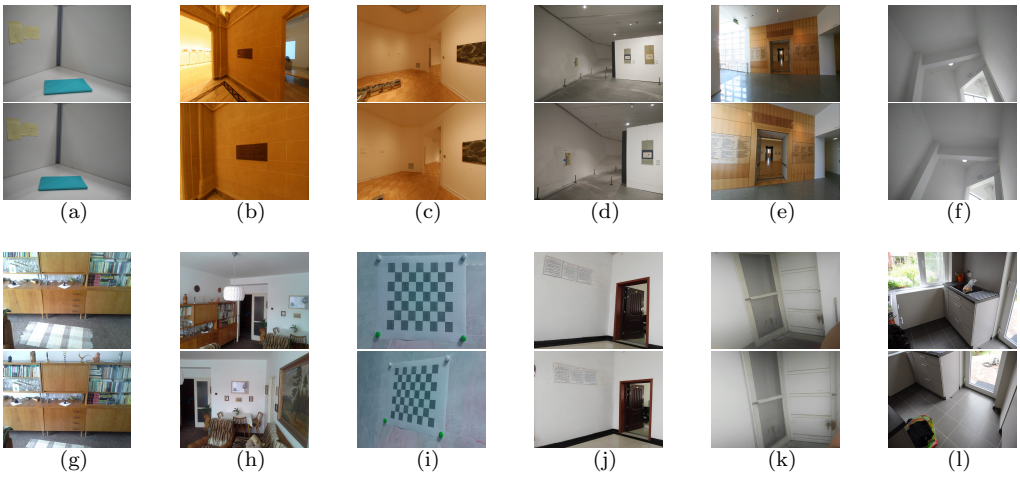

Figure 8: Several examples of the collected indoor images used for the comparison of different matching approaches.

Table 2: Comparison of different matching methods. The number of correct matches, the number of total matches and the matching accuracy of our method for comparison with the key-point matching results are reported in the first row. The results for the SIFT [10], Affine-SIFT [13,43], Hessian-Affine [44], EBR [12] and IBR [12] key-point matching approaches are listed in the 3-rd to 7-th rows. The average matching accuracy for all collected images is reported in the last column.

Method \ Image pair		(a)	(b)	(c)	(d)	(e)	(f)	(g)	(h)	(i)	(j)	(k)	(l)	Average accuracy
Ours (Junctions)	# correct	12	26	12	16	50	14	197	65	119	37	17	33	
	# in total	12	29	13	20	60	15	214	69	121	45	19	40	**85.17%**
	accuracy (%)	**100.00**	**89.66**	**92.31**	**80.00**	**83.33**	93.33	92.06	94.20	**98.35**	**82.22**	89.47	**82.50**	
SIFT [10]	# correct	128	476	559	115	435	74	708	199	147	200	103	65	
	# in total	206	700	839	222	652	287	770	261	330	299	191	161	62.69%
	accuracy (%)	62.14	68.00	66.63	51.80	66.72	25.78	91.95	76.25	44.55	66.89	53.93	40.37	
Affine-SIFT [13]	# correct	135	183	433	364	430	119	4141	1271	136	172	196	163	
	# in total	141	240	519	480	549	133	4205	1326	240	263	224	264	82.85%
	accuracy (%)	95.74	76.25	83.43	75.83	78.32	89.47	**98.48**	**95.85**	56.67	65.40	87.50	61.74	
Hessian-Affine [44]	# correct	24	13	96	82	66	17	640	226	32	114	38	29	
	# in total	26	34	132	105	109	18	671	248	63	144	41	49	79.68%
	accuracy (%)	92.31	38.24	72.73	78.10	60.55	**94.44**	95.38	91.13	50.79	79.17	**92.68**	59.18	
EBR [12]	# correct	0	0	10	0	0	0	64	20	28	14	0	0	
	# in total	1	1	16	15	10	2	75	21	46	34	2	4	32.56%
	accuracy (%)	0.00	0.00	62.50	0.00	0.00	0.00	85.33	95.24	60.87	41.18	0.00	0.00	
IBR [12]	# correct	0	0	28	11	14	0	46	0	0	10	0	0	
	# in total	4	9	39	16	25	9	63	12	10	21	8	5	31.84%
	accuracy (%)	0.00	0.00	71.79	68.75	56.00	0.00	73.02	0.00	0.00	47.62	0.00	0.00	

5.3.1 Matching results for key-point matching algorithms

In Tab. 2, our proposed ASJ feature detector is compared with the most widely used feature detectors for key-point matching. From the perspective of key-point matching, we regard an ASJ as a key-point with two specific orientations. The matching accuracy for the ASJ approach is better than that for the other key-point matching algorithms in most cases. Representatively, in Fig. 8(i), the indistinct repeated regions of the chessboard are matched very well, with an accuracy of 98.35%, because ASJs describe corner points with more global information than other approaches, allowing their relative positions in images to be better represented with meaningful orientations.

In comparison with the most closely related approaches, the EBR and IBR detectors [12], our proposed ASJ detector can more effectively handle straight edges to produce more key-points and more correct correspondences. In many cases, as shown in Tab. 2, the EBR and IBR results demonstrate the limitations of

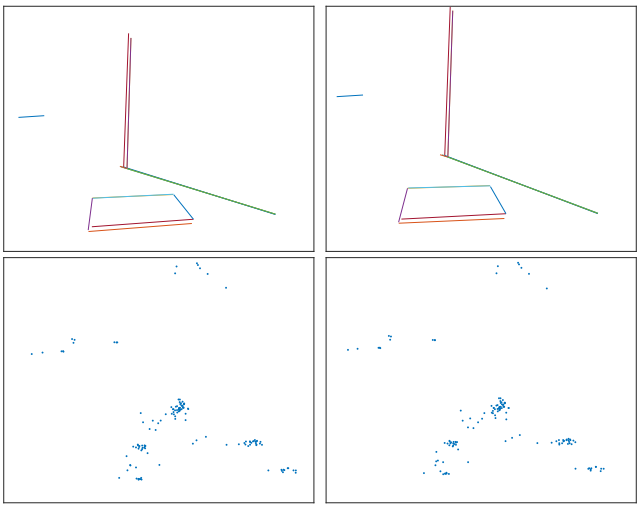

Figure 9: Top: Correctly matched ASJs for the image pair presented in Fig. 8(a). Bottom: Correctly matched key-points obtained using the Affine-SIFT algorithm [13, 43]. Although the number of correct matches for Affine-SIFT (135) is greater than that for the ASJ approach (12), the ASJ results better represent the structural information of the input image, whereas the information provided by the plotted key-points is confusing if we do not have the input image for reference.

these methods when applied to indoor images, which tend to be dominated by straight edges.

Regarding the absolute number of correct matches, the ASJ approach yields significantly fewer than the other approaches. The best approaches in terms of generating the largest number of correct matches are Affine-SIFT and SIFT. Since the junctions detected in indoor images represent the most meaningful junctions in the scene, the fact that the absolute number of junctions is less than the number of SIFT key-points is not surprising. Nevertheless, ASJs represent the structural information of a scene more compactly than key-points do. To illustrate this point, we plot the correctly matched key-points and ASJs on a clean background; the structure of the scene is well represented by the ASJs by virtue of their branches, whereas the plotted key-points are difficult to understand without their input images. As shown in Fig. 9 to Fig. 11, the relevant geometric information is well represented by a relatively small number of matched ASJs (12 for Fig. 9, 50 for Fig. 10 and 65 for Fig. 11), whereas the matched Affine-SIFT key-points show confused results even though the number of matches is much greater than for the ASJs. Several examples of matching results are shown in Fig. 13-14.

5.3.2 Matching results for line segment matching

We evaluate the line segments matched using the state-of-the-art LPI [14] and LJL [15] approaches for comparison with our method using a strict rule based on a comparison of the endpoints of corresponding line segments instead of their line equations. For the example image pairs shown in Fig. 8, our proposed method is superior to the existing methods, demonstrating a considerable advantage in most cases. The numbers of correctly matched line segments are also comparable to those of the other approaches. In addition to exhibiting the superior matching accuracy, the results of our method describe the scene more completely, as shown in Fig. 12.

In contrast to the LPI [14] and LJL [15] approaches, our approach performs better while not using any pre-estimated geometric information. As shown in Tab. 3, a key-point-driven approach to line segment matching is subject to failure because of the possibility that the geometric relationship may be erroneously estimated. For the failure case reported in Tab. 3, the image pair, as shown in Fig. 12, is dominated by

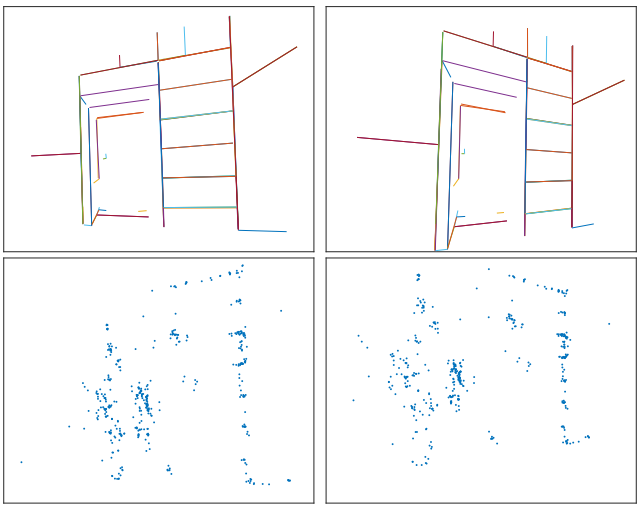

Figure 10: Top: Correctly matched ASJs for the image pair presented in Fig. 8(e). Bottom: Correctly matched key-points obtained using the Affine-SIFT algorithm [13, 43]. Although the number of correct matches for Affine-SIFT (430) is greater than that for the ASJ approach (50), the ASJ results better represent the structural information of the input image, whereas the information provided by the plotted key-points is confusing if we do not have the input image for reference.

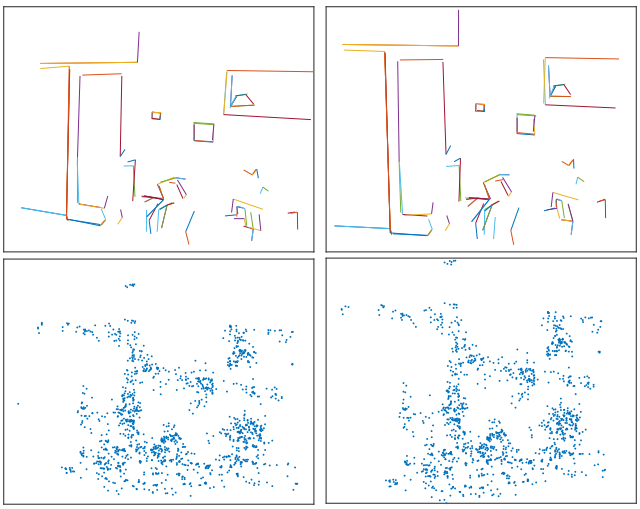

Figure 11: Top: Correctly matched ASJs for the image pair presented in Fig. 8(h). Bottom: Correctly matched key-points obtained using the Affine-SIFT algorithm [13, 43]. Although the number of correct matches for Affine-SIFT (65) is greater than that for the ASJ approach (1271), the ASJ results better represent the structural information of the input image, whereas the information provided by the plotted key-points is confusing if we do not have the input image for reference.

Table 3: Comparison of different matching methods for line segment matching. The number of correct matches is counted using the rule that the endpoints of corresponding line segments must be correct. We compare the ASJ method with the state-of-the-art LPI [14] and LJL [15] approaches and report the number of correct matches, the total number of matches and the matching accuracy. The average matching accuracy is also compared in the last column.

Method \ Image pair		(a)	(b)	(c)	(d)	(e)	(f)	(g)	(h)	(i)	(j)	(k)	(l)	Average accuracy
Ours (Line segments)	# correct	15	30	14	26	85	21	349	121	232	49	27	48	
	# in total	24	58	26	40	120	30	428	138	242	90	38	80	**71.55%**
	accuracy (%)	**62.50**	**51.72**	53.85	65.00	**70.83**	**70.00**	**81.54**	**87.68**	**95.87**	**54.44**	71.05	**60.00**	
LPI [14]	# correct	5	0	15	19	53	3	123	60	33	17	11	16	
	# in total	9	0	18	29	90	9	193	102	59	38	15	40	48.83%
	accuracy (%)	55.56	0.00	**83.33**	**65.52**	58.89	33.33	63.73	58.82	55.93	44.74	**73.33**	40.00	
LJL [15]	# correct	8	24	26	37	148	4	221	113	129	50	26	22	
	# in total	30	79	32	64	251	17	376	186	138	131	50	102	52.95%
	accuracy (%)	26.67	30.38	81.25	57.81	58.96	23.53	58.78	60.75	93.48	38.17	52.00	21.57	

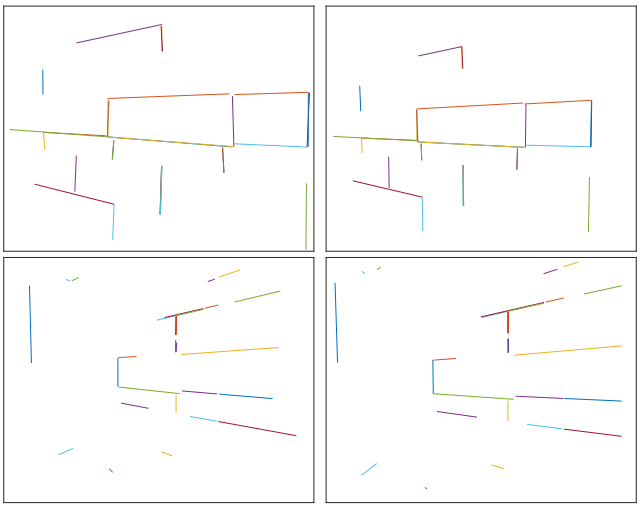

Figure 12: Matched line segments for the image pair presented in Fig. 8(b). Top: Correctly matched line segments for the ASJ method. Bottom: Correctly matched line segments for the LJL method [15]. The ASJ results describe the scene more completely, benefiting from the anisotropic scales of the junction branches.

repeated textures and a drastic viewpoint change, which are challenging for key-point matching algorithms to handle. In such a scenario, the induced epipolar geometry might be unreliable and therefore produce poor line segment matching results. By contrast, because our approach performs well in junction matching, we can use the junction correspondences to refine the line segment matching results.

6 Conclusion

In this paper, we propose a novel junction detector, called the ASJ detector, which exploits the anisotropy of junctions by estimating the endpoints (lengths) of their branches based on initially detected isotropic-scale junctions for indoor images, which are typically dominated by junctions on a global scale. We then present an affine-invariant dissimilarity measure that can be used to match the detected ASJs across different images. We test our method on a number of indoor images and compare its performance with the performance of several current state-of-the-art methods. The results demonstrate that our approach establishes a new standard for state-of-the-art performance on indoor images.

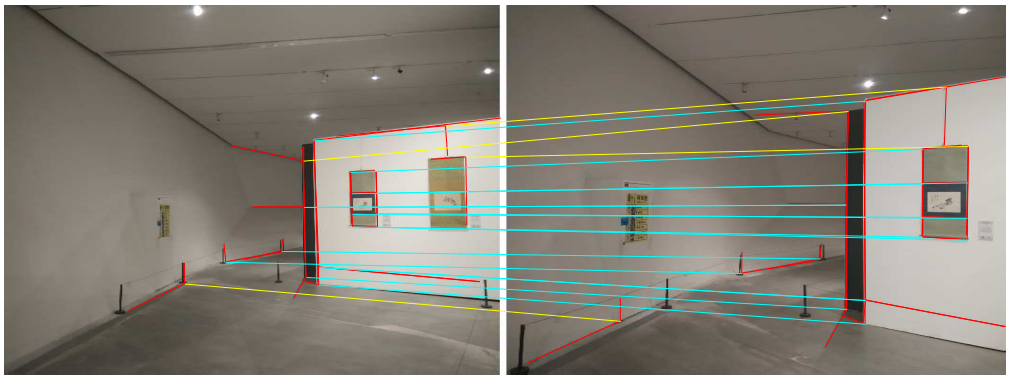

Figure 13: Matched ASJs for the image pair presented in Fig. 8(d). (# of Correct Matches, # of Total Matches) = (16, 20). False matches are connected by yellow lines, whereas correct matches are connected by cyan lines.

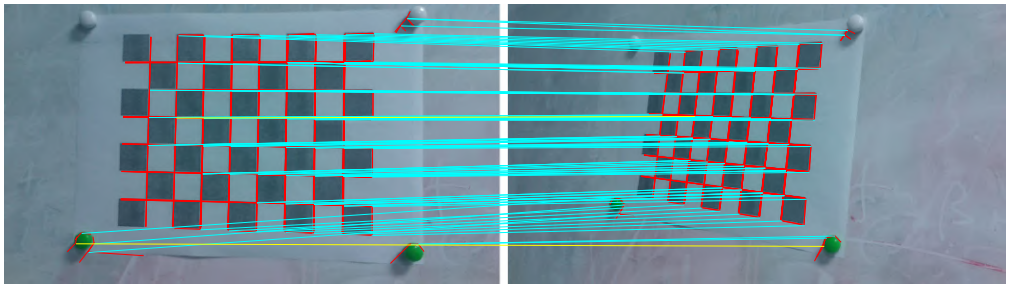

Figure 14: Matched ASJs for the image pair presented in Fig. 8(i). (# of Correct Matches, # of Total Matches) = (119, 121). False matches are connected by yellow lines, whereas correct matches are connected by cyan lines.

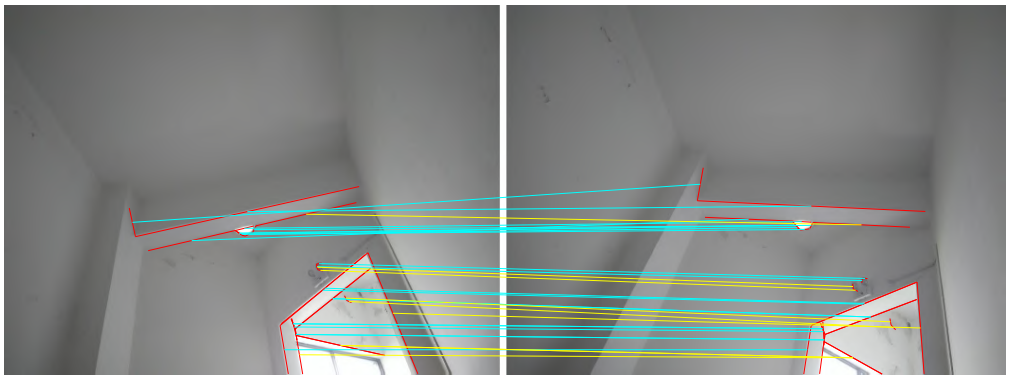

Figure 15: Matched line segments for the image pair presented in Fig. 8(f). (# of Correct Matches, # of Total Matches) = (21, 30). The midpoints of the matched line segments are connected by cyan lines (if correctly matched) or yellow lines (if mismatched).

References

[1] C. Wu, "Towards linear-time incremental structure from motion," in *3DV*, June 29 - July 1 2013, pp. 127–134.

[2] D. J. Crandall, A. Owens, N. Snavely, and D. P. Huttenlocher, "Sfm with mrfs: Discrete-continuous optimization for large-scale structure from motion," *IEEE TPAMI*, vol. 35, no. 12, pp. 2841–2853, 2013.

[3] S. Fuhrmann, F. Langguth, and M. Goesele, "MVE - A multi-view reconstruction environment," in *Eurographics Workshop on Graphics and Cultural Heritage, Darmstadt, Germany*, October 6-8 2014, pp. 11–18.

[4] P. Moulon, P. Monasse, R. Marlet, and Others, "Openmvg. an open multiple view geometry library." https://github.com/openMVG/openMVG.

[5] B. Wang, X. Bai, X. Wang, W. Liu, and Z. Tu, "Object recognition using junctions," in *ECCV*, September 5-11 2010, pp. 15–28.

[6] A. Y. S. Chia, D. Rajan, M. K. Leung, and S. Rahardja, "Object recognition by discriminative combinations of line segments, ellipses, and appearance features," *IEEE TPAMI*, vol. 34, no. 9, pp. 1758–1772, 2012.

[7] J. Yan, J. Wang, H. Zha, X. Yang, and S. M. Chu, "Multi-view point registration via alternating optimization," in *AAAI*, 2015, pp. 3834–3840.

[8] Y. Shen, W. Lin, J. Yan, M. Xu, J. Wu, and J. Wang, "Person re-identification with correspondence structure learning," in *ICCV*, December 7-13 2015, pp. 3200–3208.

[9] K. Mikolajczyk and C. Schmid, "An affine invariant interest point detector," in *ECCV*, May 28-31 2002, pp. 128–142.

[10] D. G. Lowe, "Distinctive image features from scale-invariant keypoints," *IJCV*, vol. 60, no. 2, pp. 91–110, 2004.

[11] J. Matas, O. Chum, M. Urban, and T. Pajdla, "Robust wide baseline stereo from maximally stable extremal regions," in *BMVC*, September 2-5 2002, pp. 1–10.

[12] T. Tuytelaars and L. J. V. Gool, "Matching widely separated views based on affine invariant regions," *IJCV*, vol. 59, no. 1, pp. 61–85, 2004.

[13] G. Yu and J. Morel, "ASIFT: an algorithm for fully affine invariant comparison," *IPOL Journal*, vol. 1, 2011.

[14] B. Fan, F. Wu, and Z. Hu, "Robust line matching through line-point invariants," *Pattern Recognition*, vol. 45, no. 2, pp. 794–805, 2012.

[15] K. Li, J. Yao, X. Lu, L. Li, and Z. Zhang, "Hierarchical line matching based on line-junction-line structure descriptor and local homography estimation," *Neurocomputing*, vol. 184, pp. 207–220, 2016.

[16] R. G. von Gioi, J. Jakubowicz, J. Morel, and G. Randall, "LSD: A fast line segment detector with a false detection control," *IEEE TPAMI*, vol. 32, no. 4, pp. 722–732, 2010.

[17] ——, "LSD: a line segment detector," *IPOL Journal*, vol. 2, pp. 35–55, 2012.

[18] X. Shen and P. Palmer, "Uncertainty propagation and the matching of junctions as feature groupings," *IEEE TPAMI*, vol. 22, no. 12, pp. 1381–1395, 2000.

[19] Z. Wang, F. Wu, and Z. Hu, "MSLD: A robust descriptor for line matching," *Pattern Recognition*, vol. 42, no. 5, pp. 941–953, 2009.

[20] D. Marr, "A computational investigation into the human representation and processing of visual information," *Vision*, pp. 125–126, 1982.

[21] E. H. Adelson, "Lightness perception and lightness illusions," *New Cogn. Neurosci*, vol. 339, 2000.

[22] C. Guo, S. C. Zhu, and Y. N. Wu, "Primal sketch: Integrating structure and texture," *CVIU*, vol. 106, no. 1, pp. 5–19, 2007.

[23] T. Wu, G. Xia, and S. C. Zhu, "Compositional boosting for computing hierarchical image structures," in *CVPR*, 18-23 June 2007.

[24] M. Maire, P. Arbelaez, C. C. Fowlkes, and J. Malik, "Using contours to detect and localize junctions in natural images," in *CVPR*, June 24-26 2008.

[25] E. D. Sinzinger, "A model-based approach to junction detection using radial energy," *Pattern Recognition*, vol. 41, no. 2, pp. 494–505, 2008.

[26] Z. Püspöki and M. Unser, "Template-free wavelet-based detection of local symmetries," *IEEE TIP*, vol. 24, no. 10, pp. 3009–3018, 2015.

[27] Z. Püspöki, V. Uhlmann, C. Vonesch, and M. Unser, "Design of steerable wavelets to detect multifold junctions," *IEEE TIP*, vol. 25, no. 2, pp. 643–657, 2016.

[28] G. Xia, J. Delon, and Y. Gousseau, "Accurate junction detection and characterization in natural images," *IJCV*, vol. 106, no. 1, pp. 31–56, 2014.

[29] F. Srajer, A. G. Schwing, M. Pollefeys, and T. Pajdla, "Match box: Indoor image matching via box-like scene estimation," in *3DV*, December 8-11 2014, pp. 705–712.

[30] Y. Furukawa, B. Curless, S. M. Seitz, and R. Szeliski, "Reconstructing building interiors from images," in *ICCV*, September 27 - October 4 2009, pp. 80–87.

[31] W. Förstner, "A feature based correspondence algorithm for image matching," *International Archives of Photogrammetry and Remote Sensing*, vol. 26, no. 3, pp. 150–166, 1986.

[32] C. Harris and M. Stephens, "A combined corner and edge detector," in *Alvey Vision Conference*, 1988, pp. 147–151.

[33] K. Mikolajczyk and C. Schmid, "Scale & affine invariant interest point detectors," *IJCV*, vol. 60, no. 1, pp. 63–86, 2004.

[34] W. Förstner, T. Dickscheid, and F. Schindler, "Detecting interpretable and accurate scale-invariant keypoints," in *ICCV*, 2009, pp. 2256–2263.

[35] L. Alvarez and F. Morales, "Affine morphological multiscale analysis of corners and multiple junctions," *IJCV*, vol. 25, no. 2, pp. 95–107, 1997.

[36] É. Vincent and R. Laganière, "Junction matching and fundamental matrix recovery in widely separated views," in *BMVC*, 2004, pp. 1–10.

[37] B. P. D. Ruff, "A pipelined architecture for the canny edge detector," in *Alvey Vision Conference, Cambridge, UK*, 1987, pp. 1–4.

[38] S. Ramalingam, M. Antunes, D. Snow, G. H. Lee, and S. Pillai, "Line-sweep: Cross-ratio for wide-baseline matching and 3d reconstruction," in *CVPR*. IEEE, June 8-10 2015, pp. 1238–1246.

[39] M. A. Fischler and R. C. Bolles, "Random sample consensus: A paradigm for model fitting with applications to image analysis and automated cartography," *Commun. ACM*, vol. 24, no. 6, pp. 381–395, 1981.

[40] A. Desolneux, L. Moisan, and J.-M. Morel, *From Gestalt Theory to Image Analysis: A Probabilistic Approach*, 1st ed. Springer Publishing Company, Incorporated, 2007.

[41] A. Neubeck and L. J. V. Gool, "Efficient non-maximum suppression," in *ICPR*, August 20-24 2006, pp. 850–855.

[42] K. Mikolajczyk and C. Schmid, "A performance evaluation of local descriptors," *IEEE TPAMI*, vol. 27, no. 10, pp. 1615–1630, 2005.

[43] J. Morel and G. Yu, "ASIFT: A new framework for fully affine invariant image comparison," *SIAM J. Imaging Sciences*, vol. 2, no. 2, pp. 438–469, 2009.

[44] M. Perdoch, O. Chum, and J. Matas, "Efficient representation of local geometry for large scale object retrieval," in *CVPR*, June 20-25 2009, pp. 9–16.